
Article:
Senstius, Mads, Nielsen, Stefan Kragh and Vann, Roddy orcid.org/0000-0002-3105-2546 (2021) Trapped upper hybrid waves as eigenmodes of non-monotonic background density profiles. Plasma Physics and Controlled Fusion. 065018. ISSN: 1361-6587

https://doi.org/10.1088/1361-6587/abf85a

Trapped upper hybrid waves as eigenmodes of non-monotonic background density profiles

Trapped upper hybrid waves as eigenmodes of non-monotonic background density profiles

M G Senstius[1], S K Nielsen[1], R G L Vann[2]

[1]Department of Physics, Technical University of Denmark, Fysikvej, DK-2800 Kgs. Lyngby, Denmark

[2]York Plasma Institute, Department of Physics, University of York, York YO10 5DD, United Kingdom

Abstract. Non-monotonic plasma density structures such as blobs and magnetic islands give rise to trapped upper hybrid (UH) waves. Trapped UH waves which satisfy Bohr-Sommerfeld quantization can be thought of as eigenmodes of a cavity. Using fully kinetic particle-in-cell (PIC) simulations, we verify the existence of these UH eigenmodes and demonstrate their significance as only eigenfrequencies become unstable to three-wave interactions. The eigenmodes can be excited through parametric decay instabilities (PDIs) of an X-mode pump wave at approximately twice the UH frequency, as could be the case for a gyrotron beam traversing a blob in a magnetically confined fusion plasma. We derive a closed expression for the wavenumber of UH waves, which is accurate both close to the UH layer and to the electron cyclotron resonance. This allows for fast analysis of eigenmodes in a non-monotonic structure. An expression for the amplification of PDI daughter waves in an inhomogeneous plasma is extended to a decay region where the first several derivatives vanish. From the amplification in a convective PDI, we estimate the growth rate of the absolute PDI involving the trapped waves. We show that the excitation of eigenmodes through PDIs in our simulations are indeed absolute rather than convective due to the trapping of the daughter waves. Additionally, we show that only eigenmodes get excited through the PDIs, and that we are able to predict the growth rates of the daughter waves and how they scale with the pump wave intensity. This is evidence supporting a fundamental assumption of analytical theory describing low threshold strong scattering observed in magnetically confined fusion experiments during second harmonic electron cyclotron resonance heating (ECRH). Such low threshold instabilities can degrade ECRH performance but also offer novel uses for ion heating or as diagnostics.

Submitted to: *Plasma Phys. Control. Fusion*

1. Introduction

Unstable nonlinear three-wave interactions known as parametric decay instabilities (PDIs) occur typically when a strong pump wave is injected into a nonlinear medium. The pump wave can interact with and transfer energy to a pair of thermally excited daughter waves if certain selection rules are satisfied. PDIs are known to occur in many physical systems, including in nonlinear optics[1] and in fluids[2, 3]. In fusion plasma physics, early works[4, 5, 6, 7, 8, 9] showed that PDIs in inhomogeneous fusion plasmas, where daughter waves were convected out of the interaction region, were of little concern to electron cyclotron resonance heating (ECRH) schemes as the heating beam sources were simply not able to provide power levels above the high pump power thresholds. Known exceptions were at certain resonances such as the upper hybrid (UH) layer[10], where wave amplification[11] could lead to sufficient wave power density to overcome PDI thresholds, which is how PDIs were first observed in tokamaks[12] and stellarators[13]. The UH layer is not easily accessible for externally launched microwaves, so PDIs have generally been of little concern when using ECRH schemes, particularly for heating at the second harmonic electron cyclotron (EC) resonance.

In the last decades, the output of high power gyrotrons has reached a level where signatures of PDIs are being observed[14, 15] during second harmonic ECRH experiments. This happens even though traditional thresholds for PDI in inhomogeneous plasmas suggest that the gyrotron beams are still by far not strong enough to become unstable. The observed signatures have therefore sometimes been referred to as anomalous scattering. Analytical models[16, 17, 18, 19, 20, 21, 22, 23] were formulated to explain the scattering as the result of many consecutive PDIs involving trapped UH waves in non-monotonic density structures. While the majority of the implicated waves are found near the UH frequency, the pump wave that starts the cascades is instead near the second harmonic UH frequency. A 2nd harmonic ECRH beam injected from the low field side will always have to pass the 2nd harmonic UH layer first and is therefore at risk of these cascades of PDIs if the UH daughter waves are trapped. UH waves can be trapped in non-monotonic density structures when they are surrounded by an UH layer. The trapping leads to eigenmodes as some waves interfere constructively with themselves when they have performed a roundtrip in the non-monotonic density structure, acting as a cavity for the waves. The trapping of daughter waves means that the PDIs can become absolute rather than convective. Eigenmodes are therefore fundamental to the analytical theory describing low threshold PDIs in non-monotonic structures. It is believed that the experimentally observed scattering is not generated directly but results from subsequent PDIs where the trapped UH waves interact with ion waves and then recombine into escaping waves near the 2nd harmonic UH frequency. The PDI absorption of an ECRH beam passing through the structure may be highly dynamical due to the many different instabilities feeding off of each other. As a result of the many PDIs, the heating power intended for an entirely different region of the plasma will deteriorate. Analytical estimates for plasma

parameters taken from the TEXTOR tokamak predict that 60% 2nd harmonic ECRH power[22] was converted into undesired waves in unintended regions due to PDIs near the 2nd harmonic UH layer. Experiments in the linear device Granit[24] have shown a 45% absorption rate due to PDIs. It is also possible that models can explain unpredictable power deposition profiles[25], as well as observations of hot ions during ECRH[26, 27], since some daughter waves may accelerate ions. Excitation of trapped UH waves, i.e. slow X-mode and electron Bernstein waves (EBWs), in non-monotonic density profiles have previously been studied using fully kinetic simulations[28] but eigenmodes were not appreciated as being important, leaving the possibility open that the observations were simply the result of convective PDIs in inhomogeneous plasma density profiles, which did not actually need the trapping for instabilities to occur.

In this article, we investigate the anatomy of UH eigenmodes in non-monotonic plasma density structures and how they affect the excitation of waves inside the structure through PDIs. This is relevant to 2nd harmonic ECRH, in particular if the ECRH beam passes such a non-monotonic structure near the 2nd harmonic UH layer. The main goal is to provide evidence of UH eigenmodes and their significance in the low threshold PDIs described in analytical models such as [16, 17, 18, 19, 20, 21, 22, 23]. The evidence is in the form of fully kinetic simulations with minimal assumptions about how the plasma behaves. In section 2, we introduce the UH eigenmodes and derive a dispersion relation to describe them. We analyze the eigenmodes in a 1D super-Gaussian density profile as well as the frequencies that can be excited through PDIs at the fairly homogeneous top of the density profile. The analytical theory describing convective PDI is extended to accommodate the vanishing derivatives at the top of the density profile. A convective PDI occurs when the instability is limited to a finite decay region which a pump wave passes through a limited number of times. This produces a finite amplification of the PDI daughter waves. An absolute PDI, on the other hand, is an instability where the daughter waves grow exponentially in time such as in a homogeneous medium where the waves never leave the decay region. Estimates of convective versus absolute PDI show that convective PDI will produce barely noticeable amplification whereas excitation of eigenmodes will result in an instability with a growth rate comparable to that of the corresponding homogeneous instability. In section 3, we use a fully kinetic particle-in-cell (PIC) code to investigate the eigenmodes numerically. The PIC simulations are entirely independent of the analytical derivations and serve as a numerical validation of them. First, the eigenmode spectrum of a super-Gaussian is compared to the predictions from section 2. Then, an X-mode pump wave is added to show that the predicted PDI daughter wave frequencies can be excited. The X-mode pump wave is close the to 2nd harmonic UH frequency and is able to propagate throughout the domain, whereas the eigenmodes are of lower frequency and are trapped between multiple UH layers. Next, the width of the density profile is varied to demonstrate that PDI daughter waves are only excited when they both coincide with eigenfrequencies of the cavity and that the amplification is much greater than a convective PDI would produce. Lastly, a scan of pump wave intensities is compared to the predicted scaling.

2. Theory on wave interactions and eigenmode anatomy

2.1. Parametric decay instabilities

PDIs can occur in media with a quadratic nonlinearity such a plasma described by the Boltzmann or fluid equations. The three-wave interactions causing PDIs require energy and momentum to be conserved, leading to the selection rules

$$\omega_0 = \omega_1 + \omega_2, \tag{1}$$

$$\mathbf{k}_0 = \mathbf{k}_1 + \mathbf{k}_2, \tag{2}$$

where ω_j is the angular frequency of the j^{th} wave and k_j is its wave vector, with index 0 referring to a strong pump wave and indices 1 and 2 to its PDI daughter waves. In a homogeneous medium, PDIs that satisfy the selection rules can become absolutely unstable and grow exponentially in time if the interaction rate exceeds the losses of the daughter waves. In an inhomogeneous and monotonic medium, the daughter waves will experience a finite amplification as they traverse a decay region where the selection rules are approximately satisfied, also called a convective instability.

2.2. Dispersion relations

In this investigation, an electromagnetic X-mode wave is injected into a 1D plasma and interacts with electrostatic plasma modes near the 2nd harmonic UH layer. A simple cold description is used for the pump wave whereas the daughter waves require a more complicated treatment. Their description is obtained by merging two asymptotic expressions. This section is split into several parts dealing with each step.

The pump wave is described as a cold X-mode wave

For the pump wave, the cold plasma description of an electromagnetic X-mode wave will suffice. Its wavenumber is given by

$$k_0 = \frac{\omega_0}{c}\sqrt{1 - \frac{\omega_{\text{pe}}^2}{\omega_0^2}\frac{\omega_0^2 - \omega_{\text{pe}}^2}{\omega_0^2 - \omega_{\text{UH}}^2}}, \tag{3}$$

where $\omega_{\text{pe}}^2 \equiv e^2 n_e/(\varepsilon_0 m_e)$, $\omega_{\text{ce}} \equiv eB/m_e$, $\omega_{\text{UH}}^2 \equiv \omega_{\text{pe}}^2 + \omega_{\text{ce}}^2$, c is the speed of light in vacuum, e is the elementary charge, ε_0 is the vacuum permittivity, m_e is the electron mass, n_e is the electron density and B is the magnetic field.

Small wavenumber approximation for UH waves

For the UH waves, things are more complicated. First, an expression valid for small wavenumbers must be found. For this low-dimensionality study, we describe the UH waves using the warm electrostatic dispersion relation. Neglecting the ion response and collisional damping, the electrostatic dispersion relation for EBWs is given in [29] by

$$k_j^2 - 2k_j^2 \frac{e^{-\lambda_e}}{\lambda_e} \sum_{n=1}^{\infty} I_n(\lambda_e) \frac{n^2 \omega_{\text{pe}}^2}{\omega_j^2 - n^2 \omega_{\text{ce}}^2} = 0, \tag{4}$$

where $\lambda_e \equiv k_j^2\rho_{\mathrm{Le}}^2/2$ is an expansion parameter to be used, $\rho_{\mathrm{Le}}^2 \equiv 2m_eT_e/(e^2B^2)$ is the electron Larmor radius, T_e is the electron temperature in units of energy and I_n is the modified Bessel function of the first kind. Whilst equation (4) describes EBWs well, it is computationally slow to solve numerically for a large range of parameters and we therefore seek to simplify it. For most applications, it suffices to expand the second term to second order in λ_e, i.e. the factor of k_j^2 and then a first order expansion in λ_e of the rest of the term. However, we will need a better approximation closer to the electron cyclotron resonances where $k_j \to \infty$ in order to calculate the eigenfrequencies with a better precision. The approach will be to combine a higher order expansion with an asymptotic relation. We start by expanding the expression to fourth order in λ_e. To achieve this, we recall the definition $I_n(\lambda_\mathrm{e}) = \sum_{m=0}^{\infty}(\lambda_\mathrm{e}/2)^{2m+n}/(m!(m+n!))$ for integer n. This means that we can use the expansions $I_1(\lambda_\mathrm{e}) \approx \frac{\lambda_\mathrm{e}}{2} + \frac{\lambda_\mathrm{e}^3}{16}$, $I_2(\lambda_\mathrm{e}) \approx \frac{\lambda_\mathrm{e}^2}{8} + \frac{\lambda_\mathrm{e}^4}{96}$, $I_3(\lambda_\mathrm{e}) \approx \frac{\lambda_\mathrm{e}^3}{48}$, $I_4(\lambda_\mathrm{e}) \approx \frac{\lambda_\mathrm{e}^4}{384}$, $I_n(\lambda_\mathrm{e}) \approx 0$ for $n > 4$, and $e^{-\lambda_\mathrm{e}} \approx 1 - \lambda_\mathrm{e} + \frac{\lambda_\mathrm{e}^2}{2} - \frac{\lambda_\mathrm{e}^3}{6}$ to obtain

$$\ell_{\mathrm{Te},3}^6 k_j^8 + \ell_{\mathrm{Te},2}^4 k_j^6 + \ell_{\mathrm{Te},1}^2 k_j^4 + Sk_j^2 = 0, \tag{5}$$

where $S \equiv 1 - \frac{\omega_{\mathrm{pe}}^2}{\omega_j^2 - \omega_{\mathrm{ce}}^2}$ and the length scales $\ell_{\mathrm{Te},n}$ have been defined as

$$\ell_{\mathrm{Te},n}^{2n} \equiv -\frac{2\omega_{\mathrm{pe}}^2}{\omega_{\mathrm{ce}}^2\rho_{\mathrm{Le}}^2}\prod_{n'=1}^{n+1}\frac{(2n'-1)\omega_{\mathrm{ce}}^2\rho_{\mathrm{Le}}^2}{2(\omega_j^2 - n'^2\omega_{\mathrm{ce}}^2)}. \tag{6}$$

We see that $\ell_{\mathrm{Te},0} = S - 1$ but the exponent breaks the series as $\ell_{\mathrm{Te},0}^{2\cdot 0} = 1$, of course. A different definition of the coefficients is possible but this notation is chosen to keep in line with related literature where $\ell_{\mathrm{Te},1}$ is often used. The original dispersion relation in equation (4) is based on an electrostatic approximation which is not valid for small λ_e. We want a solution that connects to X-mode for small λ_e and behaves as the cold plasma X-mode far from the UH layer so as argued in[23], we add to our dispersion relation a zeroth order term of $-\frac{\omega_j^2}{c^2}(S^2 - D^2)$ where $D \equiv \omega_{ce}\omega_{\mathrm{pe}}^2/[\omega_j(\omega_j^2 - \omega_{\mathrm{ce}}^2)]$ to obtain the resulting dispersion relation

$$\mathcal{D} \equiv \ell_{\mathrm{Te},3}^6 k_j^8 + \ell_{\mathrm{Te},2}^4 k_j^6 + \ell_{\mathrm{Te},1}^2 k_j^4 + Sk_j^2 - \frac{\omega_j^2}{c^2}(S^2 - D^2) = 0. \tag{7}$$

This result may also be obtained by starting with the full hot plasma dispersion relation from [29] instead of equation (4). In that case, there is no need to add the cold X-mode contribution but the calculations are longer because a lot of small terms have to be neglected in order to ultimately get the fairly compact expression above. The obtained dispersion relation is biquartic in k_j and can be solved for k_j^2 using Ferrari's method. Whereas a quadratic equation has a rather simple solution familiar to many people, the solution to a quartic equation is much more extensive, so we introduce the following quantities in order to be able to write the solutions more compactly

$$\alpha_1 \equiv \frac{8\ell_{Te,3}^6\ell_{Te,1}^2 - 3\ell_{Te,2}^8}{8\ell_{Te,3}^{12}}, \tag{8}$$

$$\alpha_2 \equiv \frac{\ell_{Te,2}^{12} - 4\ell_{Te,3}^6\ell_{Te,2}^4\ell_{Te,1}^2 + 8\ell_{Te,3}^{12}S}{8\ell_{Te,3}^{18}}, \tag{9}$$

$$\Delta_0 \equiv \ell_{Te,1}^4 - 3S\ell_{Te,2}^4 - 12\ell_{Te,3}^6\frac{\omega^2}{c^2}(S^2-D^2), \tag{10}$$

$$\Delta_1 \equiv 2\ell_{Te,1}^6 - 9S\ell_{Te,2}^4\ell_{Te,1}^2 - 27\ell_{Te,2}^8\frac{\omega^2}{c^2}(S^2-D^2) + 27\ell_{Te,3}^6S^2 + 72\ell_{Te,3}^6\ell_{Te,1}^2\frac{\omega^2}{c^2}(S^2-D^2), \tag{11}$$

$$C \equiv \left[\frac{\Delta_1 + \sqrt{\Delta_1^2 - 4\Delta_0^3}}{2}\right]^{1/3}, \tag{12}$$

$$Q \equiv \frac{1}{2}\sqrt{-\frac{2}{3}\alpha_1 + \frac{1}{3\ell_{Te,3}^6}\left[C + \frac{\Delta_0}{C}\right]}. \tag{13}$$

With this, Ferrari's method[30, 31] gives the four solutions to the squared wave number as

$$k_{\perp,\pm_1,\pm_2}^2 = -\frac{\ell_{Te,2}^4}{4\ell_{Te,3}^6} \mp_2 Q \pm_1 \frac{1}{2}\sqrt{-4Q^2 - 2\alpha_1 \pm_2 \frac{\alpha_2}{Q}}, \tag{14}$$

where $\pm_1$ and $\pm_2$ are two signs that can be chosen in a total of 4 diffent ways, and $\mp_2 = -\pm_2$. For each of these 4 choices of signs there are 2 solutions, i.e. $\pm k_{\perp,\pm_1,\pm_2}$ which differ only by their direction of propagation. The solutions are rather extensive expressions so to check that they are indeed solutions to equation (7), we expand the factorized polynomial

$$\ell_{Te,3}^6(k_j^2 - k_{\perp,+,+}^2)(k_j^2 - k_{\perp,+,-}^2)(k_j^2 - k_{\perp,-,+}^2)(k_j^2 - k_{\perp,-,-}^2) = 0, \tag{15}$$

which must be identical to equation (7) if $k_{j,\pm_1,\pm_2}$ have been determined correctly. We use the mathematical software Maple to verify that the initial coefficients can be recovered by inserting the found solutions

$$-\ell_{Te,3}^6\sum_\mu k_{\perp,\mu}^2 = \ell_{Te,2}^4, \tag{16}$$

$$\ell_{Te,3}^6\sum_{\mu,\nu} k_{\perp,\mu}^2 k_{\perp,\nu}^2 = \ell_{Te,1}^2, \tag{17}$$

$$-\ell_{Te,3}^6\sum_{\mu,\nu,\eta} k_{\perp,\mu}^2 k_{\perp,\nu}^2 k_{\perp,\eta}^2 = S, \tag{18}$$

$$\ell_{Te,3}^6 k_{\perp,+,+}^2 k_{\perp,+,-}^2 k_{\perp,-,+}^2 k_{\perp,-,-}^2 = -\frac{\omega_j^2}{c^2}(S^2-D^2), \tag{19}$$

where the sums are over products of the found solutions, never using the same solution for more than one index and counting all identical products only once. Maple is unable to reduce the last identity symbolically - likely because of the immense length of the left hand side - but Maple is able to verify it numerically.

The four positive solutions in equation (7) are shown in figure 1 around the first three EC harmonics when they are real. Parameters are chosen such that $\omega_{\mathrm{UH}} < 2\omega_{\mathrm{ce}}$, as will be the case in this study. The analytical interpretation of the solutions in equation (14) is difficult and, as can be seen in figure 1, the four solutions come together to form the X-mode and EBW dispersion curves in an intricate way, not a single solution accounting for any of them by itself. The part of the figure below 80 GHz accounts for the UH waves with the left part being slow X-mode and the right part is the first EBW

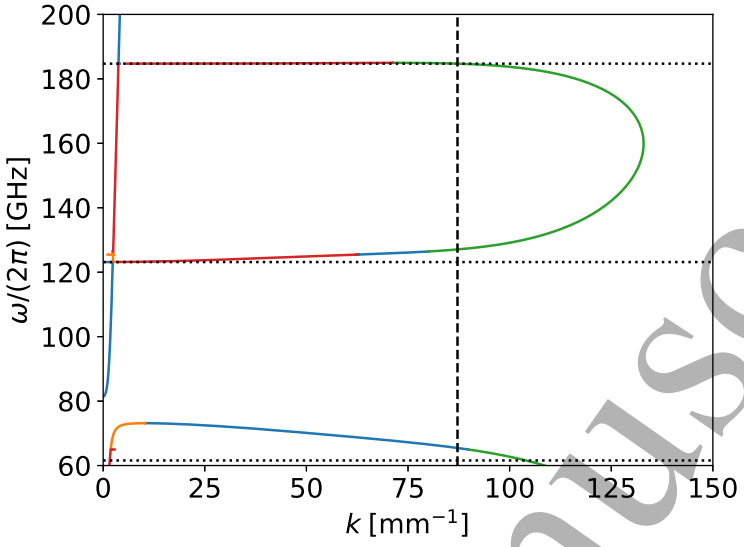

Figure 1. The solutions $k_{\perp,\pm_1,\pm_2}$ from equation (14) to the X-mode and EBW dispersion relation shown in equation (7). The blue line is $k_{\perp,+,+}$, the orange line is $k_{\perp,-,+}$, the green line is $k_{\perp,+,-}$ and the red line is $k_{\perp,-,-}$. The horizontal black dotted lines mark the first three harmonics of $\omega_{ce}/(2\pi)$, and the vertical black dashed line marks unity of the expansion parameter, i.e. $\lambda_e = 1$. Together, the solutions behave correctly when $\lambda_e < 1$ but X-mode and EBWs are not represented by a single one of the solutions. The behavior for $\lambda_e > 1$ is incorrect and motivates the need for an asymptotic expression for $\lambda_e \to \infty$. Plasma parameters for this plot are $B = 2.2$ T, $T_e = 112$ eV and $n_e = 2 \times 10^{19}$ m^{-3}, which can be realized in a device like Wendelstein 7-X[32] and will be used for the analysis of fully kinetic simulations in later sections.

branch. The point where they meet is the UH layer. Starting from around 80 GHz and up, a steep curve can be appears. This is the fast X-mode branch and it emerges from the R-cutoff. At harmonic of the electron cyclotron resonance, a more horizontal line appears which are the higher EBW branches which are valid until around the horizontal dashed line. Although each line is composed of several of the 4 solutions indicated by different colors, characterizing the different modes numerically is more straightforward; we calculate all four solutions and order them so that the smaller real solution is the X-mode solution, the second smallest real solution is the EBW solution that connects to X-mode at the UH layer, and any remaining complex or larger k_j solution is discarded. We denote the EBW solution $k^+_{j,\text{expansion}}$ and the X-mode solution k^-_j to be in line with related literature.

Large wavenumber approximation for UH waves

Even though our dispersion relation is a higher order expansion, it still assumes $\lambda_e \ll 1$. Near harmonics of the electron cyclotron resonances, we expect that $\lambda_e \to \infty$ but figure 1 shows that the solutions in equation (1) do not display this behavior properly. To get the correct asymptotic behavior near the electron cyclotron resonances, we return to equation (4) and use the asymptotic expansion[30] for $\lambda_e \to \infty$

Trapped UH eigenmodes

$$I_n(\lambda_e) \approx \frac{e^{\lambda_e}}{\sqrt{2\pi\lambda_e}} \sum_{j=1}^{\infty} \frac{(-1)^j}{j!} \prod_{0<j'\leq j} \frac{4n^2-(2j'-1)^2}{8\lambda_e}, \tag{20}$$

to obtain the equation

$$\frac{\omega_{\mathrm{ce}}^2}{2\omega_{\mathrm{pe}}^2} \approx \sum_{n=1}^{\infty} \frac{1}{\sqrt{2\pi\lambda_{\mathrm{e}}^3}} \frac{n^2\omega_{\mathrm{ce}}^2}{\omega^2-n^2\omega_{\mathrm{ce}}^2} \sum_{j=0}^{\infty} \frac{(-1)^j}{j!} \prod_{0<j'\leq j} \frac{4n^2-(2j'-1)^2}{8\lambda_e}. \tag{21}$$

Assuming that the frequency is close to the nth electron cyclotron resonance, we neglect the contribution from all other resonances and keep only the λ_e^{-1} term to obtain

$$\frac{\omega_{\mathrm{ce}}^2}{2\omega_{\mathrm{pe}}^2} \approx \frac{1}{\sqrt{2\pi\lambda_{\mathrm{e}}^3}} \frac{n^2\omega_{\mathrm{ce}}^2}{\omega^2-n^2\omega_{\mathrm{ce}}^2}, \tag{22}$$

which may be rearrange to yield an asymptotic expression for the wavenumber

$$k_{j,\mathrm{asym}} \approx \frac{1}{\rho_{\mathrm{Le}}} \left[\frac{\sqrt{\pi}\omega_{\mathrm{ce}}}{2n} \frac{\omega-n\omega_{\mathrm{ce}}}{\omega_{\mathrm{pe}}^2} \right]^{-1/3}. \tag{23}$$

Completely opposite to equation (14), this solution only describes EBWs close to the cyclotron resonances and is not accurate near the UH layer.

Merging the two limiting UH wave dispersion relations

In this study, we want a dispersion relation for the UH waves that is precise immediately at the UH layer but also closer to the cyclotron resonances without having to numerically invert the full hot plasma dispersion relation. The final step is therefore to formulate a function that has the behavior of equation (14) for small λ_e and the behavior of equation (23) for large λ_e. We will be looking at a situation where $\omega_{\mathrm{UH}} < 2\omega_{ce}$ so we set $n = 1$ in equation (23) and go for the form

$$k_j^+ = k_{j,\mathrm{expansion}}^+ \left[1-\mu\left(\frac{\omega-\omega_{\mathrm{mix}}}{\omega_{\mathrm{char}}} \right) \right] + k_{j,\mathrm{asym}}\mu\left(\frac{\omega-\omega_{\mathrm{mix}}}{\omega_{\mathrm{char}}} \right), \tag{24}$$

where $\mu(\omega) = [1-\tanh(\omega)]/2$ is our choice of a sigmoid function that connects the two limiting dispersion relations and $\omega_{\mathrm{mix}}, \omega_{\mathrm{char}}$ are characteristic frequencies which ensure that the two limiting forms are tied together properly. The mixing occurs over a frequency band of $\omega_{\mathrm{UH}} - \omega_{ce}$, so we choose a smaller characteristic frequency band of $\omega_{\mathrm{char}} = (\omega_{\mathrm{UH}} - \omega_{ce})/5$. The frequency that really separates the two solutions is when $\lambda_e = 1$ but this is not straightforward to determine so we instead pick a frequency in between the UH frequency and the cyclotron resonance, $\omega_{\mathrm{mix}} = (\omega_{\mathrm{UH}} - \omega_{\mathrm{ce}})/3 + \omega_{\mathrm{ce}}$. As can be seen in figure 2, the obtained dispersion relation is a good estimate for the full dispersion relation over many orders. It is likely that a more optimal choice of ω_{char} and ω_{mix} exists as our choice was a simple estimate to favor the asymptotic expansion only close to the EC resonance. With this dispersion relation, the computation is faster and more stable than solving equation (4) inversely using e.g. Scipy's `root` or even an optimized solver. Whilst solving the full hot plasma dispersion relation is quick when it only has to be done for a few frequencies and plasma parameters, this study will need to solve it extensively. Consequently, the analysis presented in the article is rendered

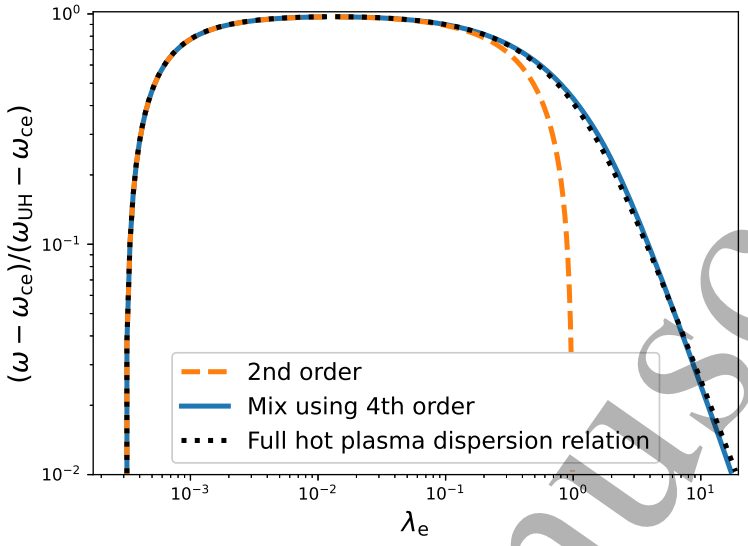

Figure 2. A comparison of UH dispersion relations over different orders of the expansion parameter $\lambda_e = (k_j \rho_{Le})^2/2$. The y-axis is the frequency shifted and normalized such that zero is the EC frequency and unity is the UH frequency. The *Full hot plasma dispersion relation* can be found in [29]. The *2nd order* line is an often employed dispersion relation, corresponding to equation (7) up to the k_j^4 term. Lastly, *Mix using 4th order* is our dispersion relation in equation (24).

not only possible but actually computationally rather cheap using a dispersion relation like equation (24).

2.3. Eigenmodes

A non-monotonic density profile will lead to multiple UH layers for UH waves in a specific frequency range. With linear conversion between X-mode and EBWs[33] as well as a change of direction of propagation, multiple UH layers trap UH waves between them; see figure 3. Waves that interfere constructively with themselves after a roundtrip in the non-monotonic region can be thought of as Bohr-Sommerfeld quantized eigenmodes[18, 34, 35] of a cavity. In 1D and within the WKB approximation, the quantization condition is

$$\int_{x_l}^{x_r} |k_m^+| - |k_m^-| \mathrm{d}x = (2m+1)\pi, \tag{25}$$

where x_l, x_r are the left and right turning points, i.e. the UH layers, of the trapped wave, m is the mode number which is a non-negative integer for eigenmodes only, and $k_m^\pm$ is the wavenumber of the associated eigenmode with + for EBW and - for X-mode. We denote the angular frequency that satisfies the quantization condition for the mth mode by Ω_m. Note that in this investigation, we consider an electromagnetic X-mode pump wave that interacts with two UH daughter waves near the 2nd harmonic UH layer. Because of this, the trapping mentioned here only applies to the daughter waves and not to the pump wave, which does not reach its UH layer.

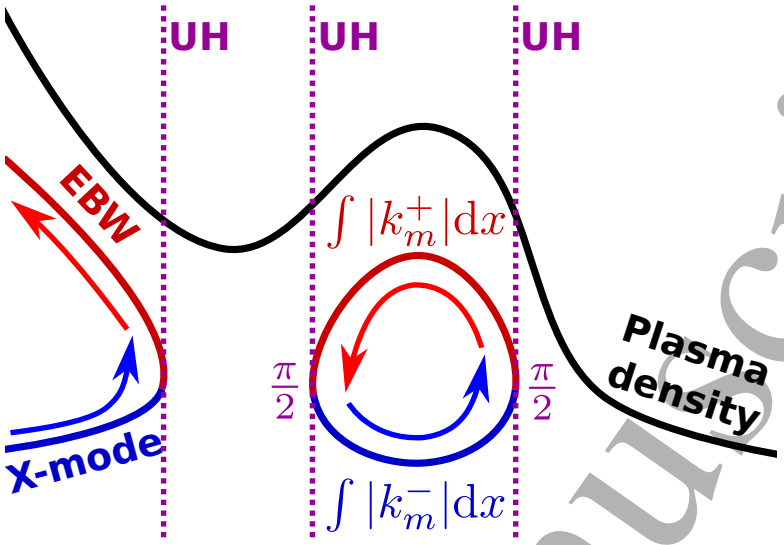

Figure 3. An illustration showing how an arbitrary non-monotonic plasma density profile can lead to trapped UH waves. The trapping mechanism is linear conversion between X-mode and EBWs at the UH layers. The non-monotonic region can act as a cavity for waves that gain an integer times 2π phase difference after a roundtrip. Term adding to the quantization condition in equation (25) are shown.

The eigenmodes are not evenly spaced in frequency and the distribution is a characteristic of the plasma parameters and spatial size of the cavity. Assuming for simplicity that the plasma parameters do not have several peaks in the cavity region, the fundamental mode is placed closest to the UH layer at its highest frequency because the integrand of equation (25) vanishes at the UH layer. Frequencies above the UH frequency do not propagate so the remaining modes are found at lower frequency. The EBW wavenumber increases towards the EC resonance where it diverges, causing the integrand in equation (25) to also diverge, which means that the eigenfrequency separation vanishes. These observations are presented in figure 4.

The eigenmodes can be excited through PDIs of an injected electromagnetic wave into two UH waves, also referred to as two-plasmon decay (TPD)[36]. For this to happen, ω and k of the eigenmodes must sum up to that of the electromagnetic pump wave. We denote the absolute difference between the possibly non-integer mode number of the j^{th} daughter wave, m_j, and its closest integer by

$$\Delta m_j \equiv |m_j - \lfloor m_j + 0.5 \rfloor| \,, \tag{26}$$

where $\lfloor m_j \rfloor$ is the floor operation or "rounding down". The sum of the differences, $\sigma_m \equiv \sum_j \Delta m_j$, is a measure of the phase mismatch after a roundtrip and should be minimized in order for daughter waves to experience smaller losses and thus a greater growth rate. Similarly, the angular frequency difference of daughter wave j and its closest eigenfrequency, $\Omega_{\lfloor m_j \rceil}$, is denoted by

$$\Delta\omega_{m_j} \equiv |\omega_j - \Omega_{\lfloor m_j \rceil}|. \tag{27}$$

We define the sum of angular frequency differences as $\sigma_\omega \equiv \sum_j \Delta\omega_{m_j}$. Although we can

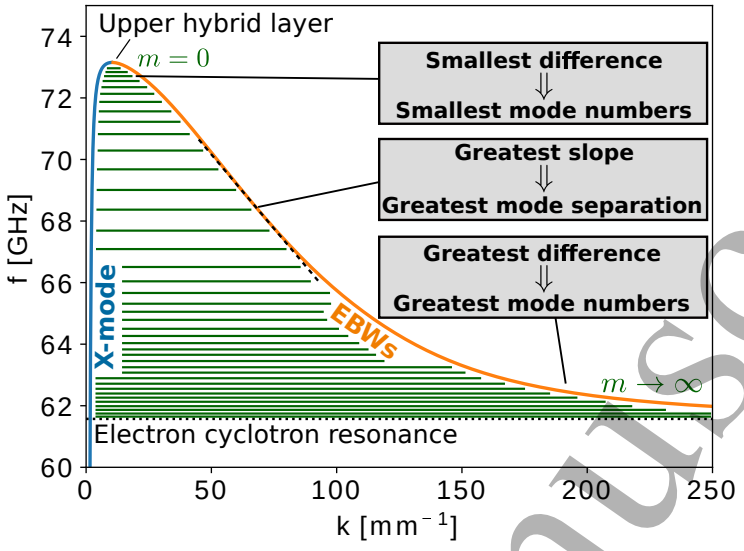

Figure 4. Characteristics of the distribution of eigenfrequencies explained through the X-mode and EBW dispersion relations. The horizontal green lines illustrate how eigenfrequencies could be distributed, note that the frequency separation is smaller near the UH and EC frequencies. The quantity m is the mode number. Plasma parameters for this plots are $B = 2.2$ T, $T_e = 112$ eV and $n_e = 2 \times 10^{19}$ m^{-3}, which are relevant to later simulations.

expect σ_ω to display the same local extrema as σ_m does, σ_ω is also going to depend on the eigenfrequency separation which is characteristic of the cavity and is not constant throughout the eigenfrequency spectrum.

2.4. TPD and eigenmodes in a super-Gaussian cavity

We now focus specifically on a 1D cavity with a homogeneous background magnetic field and a super-Gaussian density profile given by

$$n_e = n_0 \exp(-[x/\ell_{\text{cav}}]^4), \tag{28}$$

where n_0 is the peak density, and ℓ_{cav} is a characteristic length scale and measure of the width of the cavity. The choice of a super-Gaussian profile is down to its compact shape and tails that fall off quickly, which is favorable in the numerical simulation we will present in the next section. The super-Gaussian profile is not a necessity for this investigation and eigenmodes can also be observed in other density profiles, such as Gaussians. A 1D profile is chosen because EBWs with a nonzero $k_\parallel$ are highly damped, rendering them less important than those of $k_\parallel \to 0$, and the second perpendicular direction mainly obscures the analysis by adding many more eigenfrequencies and PDIs that can take place. This will make it challenging to investigate the significance of eigenfrequencies in the PIC simulations of section 3.

The super-Gaussian density profile has an almost homogeneous region in the center. PDIs that satisfy the selection rules in the center will have a long decay region compared to other PDIs and are therefore expected to have the highest growth rate; see figure

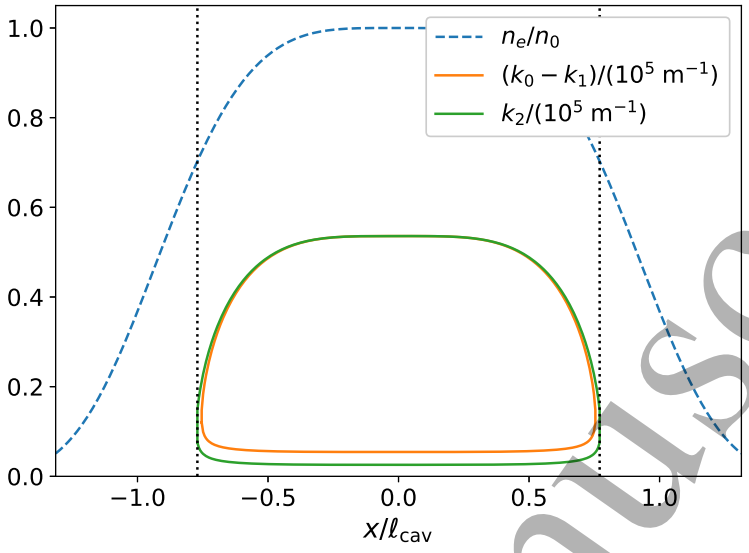

Figure 5. Demonstration of a super-Gaussian non-monotonic background density profile which supports decay of an electromagnetic $\omega_0/(2\pi) = 140$ GHz pump wave into two trapped EBWs which are trapped. The selection rules are satisfied where the solid orange and green lines overlap. The daughter waves propagate in opposite direction; $k_2 > 0$ while $k_1 < 0$. The plasma parameters are $n_e = n_0 \exp(-[x/\ell_{\mathrm{cav}}]^4)$, $n_0 = 2 \times 10^{19}$ m^{-3}, $B = 2.2$ T and $T_e = 112$ eV. Selection rules for TPD into trapped EBWs of $\omega_1/(2\pi) = 70.141$ GHz and $\omega_2/(2\pi) = 69.859$ GHz are satisfied at $x = 0$ mm.

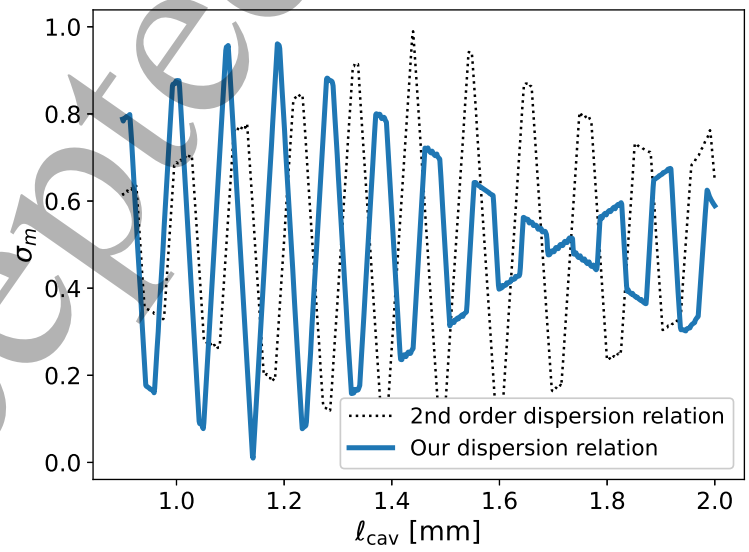

Figure 6. Sum of modenumber differences to closest integer of TPD daughter waves at the density peak; 0 would mean that both TPD daughter waves coincide perfectly with two eigenmodes; see equation (26). The envelope feature of the curve is not due to under sampling.

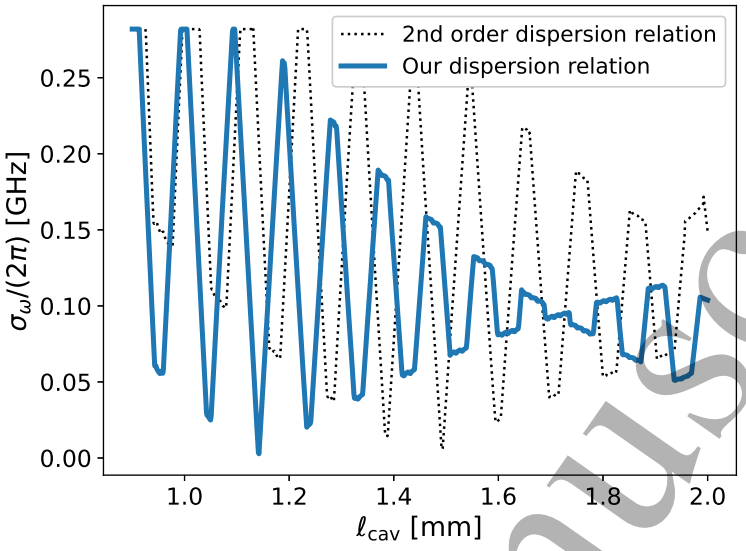

Figure 7. Sum of daughter frequency differences to closest eigenmodes of TPD daughter waves at the density peak; 0 would mean that both TPD daughter waves coincide perfectly with two eigenmodes; see equation (27). Mode spacing decreases as the cavity size is increased, causing the graph to generally decrease as the size is increased. The envelope feature of the curve is not due to under sampling.

5. Whereas the PDI matching conditions depend only on local plasma parameters, the distribution of eigenmodes depends on the parameters throughout their trapping regions as well as the extend of the trapping region. Varying only the width of the super-Gaussian cavity, the eigenfrequencies will change but the possible PDIs will not. While changing the width of any cavity shape will allow us to control the eigenfrequencies, the super-Gaussian profile allows us to neglect PDIs from anywhere but the center of the profile due to the much shorter decay regions everywhere else. However, the density profile does not need to be super-Gaussian in order for trapped waves to be excited through PDIs as was shown in [28] where also Gaussian and 2D geometries where considered. Plotting σ_m in figure 6 and σ_ω in figure 7, we see that the quantities are rather sensitive to both the cavity width as well as to the accuracy of the dispersion relation for the specific parameters. Varying ℓ_{cav} to first order will determine wether σ_m and σ_ω are at a local minimum or maximum, i.e. wether the TPD daughter waves are approximately eigenmodes or not. With this, we can investigate how the eigenmodes affect the growth of PDI daughter waves. We note that choosing a precise dispersion relation is important as the minima of the 2nd order dispersion relation turn into maxima in some places and vice versa.

The zig-zag and envelope behavior in figures 6 and 7 are the shift and separation of eigenmodes, which change as the size of the cavity is varied. Figure 8 shows the separation of eigenfrequencies normalized to the frequency difference between the TPD daughter waves in figure 5. In agreement with figure 4, figure 8 shows that the mode separation decreases towards zero as $m \to \infty$ where $\Omega_m \to \omega_{\text{ce}}$, and that the maximum

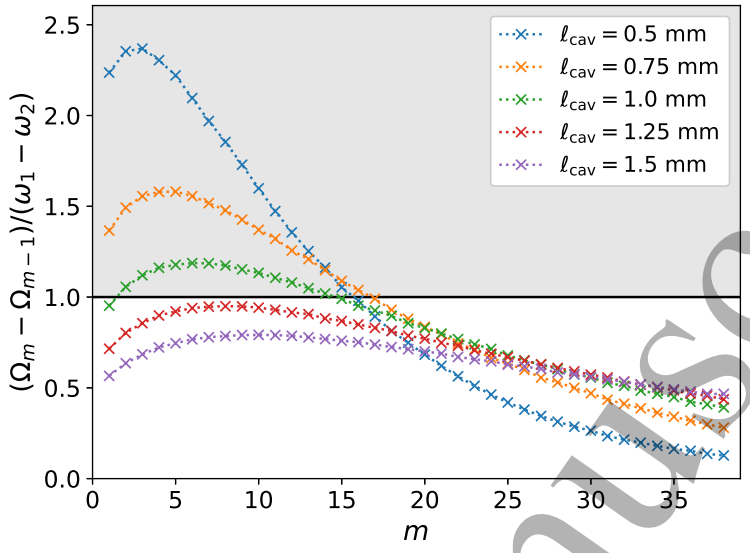

Figure 8. Separation of adjacent eigenfrequencies, normalized to the frequency difference of the TPD daughter waves in figure 5. With the normalization, greater than unity (grey region) means that TPD into eigenmodes is not possible, whereas much smaller than unity means that a quasi continuum of eigenfrequencies exists. Unity is optimal for TPD into neighboring modes, provided the shift is right. Different series refer to different cavity widths.

is generally not at the UH layer, i.e. at $m = 1$. Furthermore, narrower cavities have greater mode separation and get close to the EC frequency at a lower modenumber.

When a point in figure 8 is at unity, the mode separation is perfect for TPD into adjacent eigenmodes but there could be a frequency offset such that TPD into eigenmodes still cannot occur. Figure 9 instead shows the eigenfrequencies near the TPD daughter wave frequencies for cavity widths resulting in very similar mode separation. Still, there is a situation where the overlap is good, i.e. the blue series, and a situation where the overlap is poor, i.e. the purple series. The relative difference in cavity widths is in percents and precision is therefore key in this parameter range. This will be demonstrated in section 3. It is also possible for TPD to excite modes that are not directly adjacent but instead are separated by one or more modes. This would be the case in a larger cavity where the eigenfrequencies are closer. The slower periodic envelope feature in figures 6 and 7 may be explained by this.

2.5. TPD daughter wave growth rate estimate

The growth of PDI daughter waves is greatest in a homogeneous medium. Following [23] but neglecting linear damping, the homogeneous growth rate, γ_0, of the TPD instability is given by

$$\gamma_0^2 = |\nu_{12}\nu_{21}^*||E_0|^2, \tag{29}$$

where E_0 is the pump wave electric field amplitude and ν_{12}, ν_{21}^* are interaction coefficients which are given by lengthy expressions that can be found in chapter 4 of [23]. The

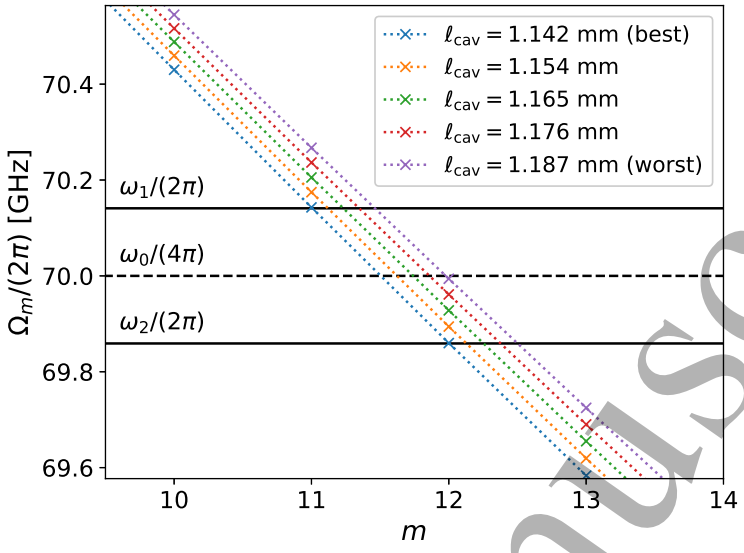

Figure 9. Eigenfrequencies near the frequencies of the TPD daughter waves in figure 5. Different series show the eigenfrequencies of cavities of slightly different sizes, where the blue line shows a situation where $\sigma_m \ll 1$, i.e. a good overlap between daughter waves and eigenfrequencies, and the purple line instead $\sigma_m \approx 1$, i.e. a poor overlap.

derivation of these coefficients is based on cold fluid equations even though the daughter waves are EBWs which are kinetic phenomena. We are going to modify the calculation by replacing the cold fluid electron mobility tensor $\mathbf{M}_{ej}$, i.e. the linear electron fluid response satisfying $\mathbf{V}_{ej,1} = -\frac{e}{m_e}\mathbf{M}_{ej}$, with the one derived from kinetic theory in chapter 5 of [29]. As the frequencies ω_j are in the EC range in this article, we neglect the ion contribution to the linear plasma current and find

$$\mathbf{M}_{ej} \approx -i\frac{\omega_j}{\omega_{pe}^2}\left[\mathbf{K}_j - \mathbf{1}\right], \tag{30}$$

where $\mathbf{K}_j$ is the hot dielectric tensor for wave j and $\mathbf{1}$ is the identity matrix. Assuming that all waves propagate parallel to the x-direction, the hot dielectric tensor has the elements $K_{j,xx} = K_{j,1}$, $K_{j,xy} = -K_{j,yx} = K_{j,2}$ and $K_{j,yy} = K_{j,1} + K_{j,0}$ to be determined. We assume that all waves are polarized perpendicularly to the magnetic field, which in [23, 29] is pointing in the z-direction, so none of the z-components of the tensor will be needed The necessary elements in the limit of $k_z \to 0$ are found to be

$$K_{j,0} = -2\frac{\omega_{pe}^2 e^{-\lambda_e}}{\omega_j}\sum_{n=-\infty}^{\infty}\lambda_e\frac{I_n(\lambda_e) - I_n'(\lambda_e)}{\omega_j + n\omega_{ce}} \tag{31}$$

$$K_{j,1} = 1 - \frac{\omega_{pe}^2 e^{-\lambda_e}}{\omega_j}\sum_{n=-\infty}^{\infty}\frac{n^2}{\lambda_e}\frac{I_n(\lambda_e)}{\omega_j + n\omega_{ce}} \tag{32}$$

$$K_{j,2} = i\frac{\omega_{pe}^2 e^{-\lambda_e}}{\omega_j}\sum_{n=-\infty}^{\infty}n\frac{I_n(\lambda_e) - I_n'(\lambda_e)}{\omega_j + n\omega_{ce}}. \tag{33}$$

The wave polarizations are also needed to calculate the interaction coefficients. For this, we again use the cold X-mode description and assume that the EBWs are fully

longitudinal. Gyrotrons installed at devices like Wendelstein 7-X are able to produce a power output of around 1 MW. Assuming a beam width of 30 mm, the average pump intensity in the center of the beam is on the order of 1 kW/mm^2. For a pump wave intensity of $I_{\mathrm{pump}} = 1$ kW/mm^2, a homogeneous growth rate of $\gamma_0 = 0.241$ ns^{-1} is obtained. Using instead the cold mobility tensor as in [23], we get a slightly higher $\gamma_{0,\mathrm{cold}} = 0.310$ ns^{-1}.

In an inhomogeneous medium, a PDI is typically convective, leading to a finite amplification of the daughter wave amplitudes, a_1 and a_2. The gain experienced by the daughter waves, $G \equiv \ln(|a_{1,\mathrm{out}}|^2/|a_{1,\mathrm{in}}|^2)$, is usually estimated as that of homogeneous PDI inside a finite decay region, where the selection rules are approximately satisfied[7, 8, 23]. This estimate relies on a first derivative of the total wavenumber mismatch, i.e. $\Delta k \equiv k_0 - k_1 - k_2$. While the super-Gaussian we are using has favorable numerical properties, its first three derivatives vanish at the top so the calculation must be adapted to our system. Following again [23], we have

$$G = 2\int_{-\infty}^{\infty} \mathrm{Re}\left(\sqrt{\frac{\gamma_0^2}{v_{\mathrm{g},1}v_{\mathrm{g},2}} - \frac{[\Delta k]^2}{4}}\right) dx', \tag{34}$$

where $v_{\mathrm{g},j}$ is the group velocity of the jth daughter wave. The integrand is only nonzero when $|\Delta k|$ is small so a Taylor expansion of Δk with respect to x up to the first nonzero term is inserted in place of Δk in the integrand. Assuming the selection rules are satisfied at $x = 0$ and denoting the number of vanishing terms before the first nonzero term of the expansion by N, the integration variable is changed to $\xi = \left[|\Delta k^{(N)}|\big|_{x=0}\sqrt{v_{\mathrm{g},1}v_{\mathrm{g},2}}/(N!\,2\gamma_0)\right]^{1/N} x$, and the integral is calculated to give

$$G_N = \delta_N \left[\frac{\gamma_0^2 \ell_{\mathrm{d},N}^2}{v_{\mathrm{g},1}v_{\mathrm{g},2}}\right]^{(N+1)/2N}. \tag{35}$$

Here $\ell_{\mathrm{d},N} \equiv |\Delta k^{(N)}|^{-1/(N+1)}\big|_{x=0}$ is the new approximate size of the decay region, and δ_N is a numerical prefactor which, through identities involving the beta function and the gamma function, can be evaluated as

$$\delta_N = \sqrt{\pi}\left[2^{N+1}N!\right]^{1/N} \frac{\Gamma\left(\frac{2N+1}{2N}\right)}{\Gamma\left(\frac{3N+1}{2N}\right)}. \tag{36}$$

In the case of $N = 1$, the plasma parameters are inhomogeneous, $\Delta k = 0$ can be satisfied but it does not occur in a local extremum of $\Delta k = 0$. This would typically be the case for inhomogeneous but monotonic plasma parameters, and equation (35) then reduces to the well known Piliya-Rosenbluth amplification of $G_1 = 2\pi\gamma_0^2\ell_{\mathrm{d},1}^2/(v_{\mathrm{g},1}v_{\mathrm{g},2})$, where $G_1 \propto I_{\mathrm{pump}}$. For $N = 2$, the selection rules are satisfied in an extremum of $\Delta k = 0$ which could be the case for non-monotonic plasma parameters. In the case of $N \gg 1$, the plasma parameters are approximately homogeneous and we see that $G_{N\gg1} \propto \gamma_0 \propto I_{\mathrm{pump}}^{1/2}$. For PDI at the top of the super-Gaussian profile, $N = 4$ and the numerical prefactor becomes $\delta_4 \approx 9.801$. For the plasma parameters and daughter waves in figure 5, the length of the decay region is $\ell_{\mathrm{d},4} = 0.432\ell_{\mathrm{cav}}$. We choose a cavity size of $\ell_{\mathrm{cav}} = 1.142$ mm, corresponding to good overlap between TPD daughter waves

and eigenmodes but ignore the trapping momentarily. The gain of the daughter waves of the TPD instability in figure 5 is then $G_4 = 1.20$, using again a pump wave intensity of $I_{\text{pump}} = 1\ \text{kW/mm}^2$. This means that the amplitudes of thermally excited waves would amplify by a factor $|a_{1,\text{out}}| = 1.82|a_{1,\text{in}}|$ after a single pass through the decay region. Without trapping, this amplification would not produce any significant effect on waves at the level of thermal noise. We note that evaluating the integral in equation (34) numerically but without inserting the Taylor expansion offers a small 3% correction to G_4 for these parameters.

With a cavity size of $\ell_{\text{cav}} = 1.142$ mm, we expect the TPD daughter waves to be trapped leading to an absolute instability. As a very simple model, we assume that the TPD instability couples perfectly to two eigenmodes and that the eigenmodes amplify as they would in a convective instability but do so once every roundtrip. This leads to the growth rate of $\gamma_j = G/\tau_j$, where τ_j is the time it takes the jth daughter waves to perform a roundtrip. The bounce times are calculated as $\tau_j = \int_{x_l}^{x_r} |\partial k_j^+/\partial\omega_j| + |\partial k_j^-/\partial\omega_j| dx$, which is evaluated numerically assuming a grid spacing of $\Delta x = 6.25 \times 10^{-3}$ mm as will be the case for the simulations in section 3. For the parameters used up until this point, the two TPD daughter waves have growth rates of $\gamma_1 = 0.328\ \text{ns}^{-1}$ and $\gamma_2 = 0.347\ \text{ns}^{-1}$, which are slighter larger than the homogeneous growth rate. Using again the cold fluid mobility tensor, even greater growth rates of $\gamma_{1,\text{cold}} = 0.449\ \text{ns}^{-1}$ and $\gamma_{2,\text{cold}} = 0.475\ \text{ns}^{-1}$ are obtained.

It can be argued that the super-Gaussian is an artificial density profile and that the expression in equation (35) is unnecessary to extend to arbitrary N when considering physical plasmas. Still, if a non-monotonic density structures can trap UH waves, then it will have a point where the first derivative of Δk vanishes and less idealized profiles could have inflection points where the first two derivatives vanish. We also note that $\gamma_j \propto G_N/\tau_j$ is in agreement with earlier studies using PIC simulations of PDIs involving trapped UH waves[28]. In the cited article, the daughter waves were confined to an essentially homogeneous region and their growth rates scaled as the square root of the pump wave intensity. By having $\gamma_j \propto G_N/\tau_j$, we notice that decay into a pair of EBWs will have a higher growth rate than for decay into one or two X-mode waves. This is because EBWs are usually slower than X-mode waves and $G_N \propto (v_{\text{g},1}v_{\text{g},2})^{-(N+1)/2N}$, still, both perform the roundtrip as an X-mode wave one way and as an EBW the other so τ_j and losses are independent of the daughter wave type. This could explain why decay into EBWs was seen to grow faster in the same study [28].

Lastly, we note that the non-monotonic density structures considered in this article are quite small compared to e.g. blobs found in ASDEX Upgrade which can be almost a factor 10 wider. For the same plasma parameters but for a width of $\ell_{\text{cav}} \approx 8$ mm, which is a common blob size in ASDEX Upgrade H-mode plasmas[37], even the local maximum of the frequency mismatch is $\max_{\ell_{\text{cav}} \approx 8\ \text{mm}} \left(\frac{\sigma_\omega}{2\pi}\right) \approx 0.04$ GHz. This is comparable to some of the local minima for the smaller structures in figure 7 because the eigenfrequencies are separated by a smaller frequency shift. Furthermore, losses due to tunneling at the turning points decrease exponentially with the Budden parameter[38, 39], i.e. the

normalized tunneling distance, and the decay regions are larger. As a consequence, a pair of eigenmodes is more likely to be excited in larger structures. The reason for choosing comparably small $\ell_{\rm cav}$ is that we intend to provide evidence that the eigenmodes exist and that the threshold for exciting trapped waves is greatly reduced if they are eigenmodes. Furthermore, choosing larger cavity sizes would make the simulations in the next section computationally much more expensive as they would require both larger domains but also longer simulations in order to get an adequate frequency resolution.

3. Particle-in-cell simulations of eigenmodes and PDI

3.1. Setup

We use the particle-in-cell (PIC) code EPOCH[40, 41, 28, 42] to simulate TPD into UH waves which are trapped in a 1D non-monotonic background density bump. Several simulations are performed with all plasma parameters kept constant except for the width of the density bump. This allows us to investigate the importance of the eigenmode structure when exciting trapped daughter waves inside a cavity. In particular we want to see if σ_m and σ_ω in figures 6 and 7 are reflected in the excited spectra. The density profiles are all super-Gaussians on the form of equation (28), with a peak density of $n_0 = 2 \times 10^{19}$ m^{-3}. The plasma consists of electrons and deuterons, both with the same initial super-Gaussian density profile. The electron and ion temperature are both $T_{\rm e} = T_{\rm i} = 100$ eV, which is slightly lower than the figures in the previous section. This is because the wave spectra obtained in EPOCH suggest that the temperature is slightly higher than what EPOCH evaluates the temperature to be. The temperature adjustment will be argued for in figure 11. The background magnetic field is chosen to be $B = B_y = 2.2$ T and the pump frequency is $\omega_0/(2\pi) = 140$ GHz. For these parameters, half frequency waves are above the EC frequency, $\omega_{\rm ce}/(2\pi) = 61.57$ GHz, and the electron plasma frequency, $\omega_{\rm pe}/(2\pi) = 40.16$ GHz, while being close to yet below the UH frequency, $\omega_{\rm UH}/(2\pi) = 73.51$ GHz. These parameters do not model particular experimental values but could be achieved in a device like the Wendelstein 7-X[32]. The exact choice of density, magnetic field and temperature profiles is not vitally important as long as the pump wave is below the 2nd harmonic UH layer and can decay into two trapped daughter waves. Here, the trapping is achieved solely through an inhomogeneous density profile but it could also be achieved by varying the magnetic field or the temperature as they affect the UH layer. From a numerical point of view, a low temperature is undesirable as the wavenumbers of the EBWs are larger, making the simulations more costly and an inhomogeneous background magnetic field is not possible in 1D EPOCH simulations. For all simulations, we use a grid with -1.5 mm $\leq x \leq 1.5$ mm and $n_{\rm x} = 480$ grid points in order to have sufficient spatial resolution for the EBWs in the vicinity of $\omega_0/2$. We use $n_{\rm part} = 1000 n_{\rm x}$ superparticles for each of two particle species. Because the superparticles are picked randomly from a Maxwellian distribution, the initial temperature is not completely uniform and may

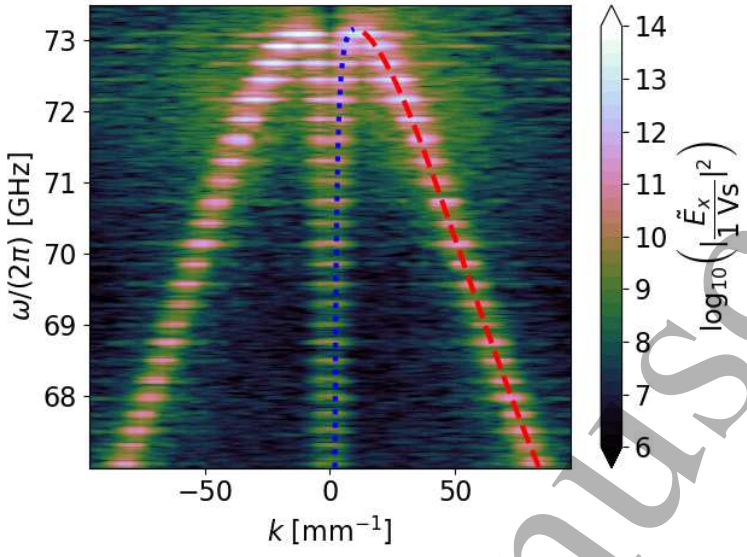

Figure 10. Spectrum immediately below the UH frequency. Rather than solid dispersion lines, distinct peaks corresponding to frequencies where trapped waves satisfy quantization conditions are clearly visible along the X-mode and EBW dispersion curves. The size of the cavity is $\ell_{\text{cav}} = 1.142$ and the FFT window is -0.75 mm $< x < 0.75$ mm, 1 ns $< t <$ 69 ns. The dotted blue line and dashed red line are the X-mode and EBW dispersion relations from section 2 at $T_e = 112$ eV.

further develop throughout the simulations due to collisional damping of the trapped waves. This also leads to thermally excites waves. For the fields, open boundary conditions are used. Particles exiting through the boundaries are replaced by thermally distributed ones entering the domain. The pump wave is excited as X-mode at the left $x = -1.5$ mm boundary and is not prescribed throughout the domain. The time step is 0.95 of the longest step allowed by the Courant stability criterion[43], resulting in a time step of $\Delta t \approx 2 \times 10^{-5}$ ns.

3.2. Eigenmode spectrum without a pump wave

We run a simulation for 70 ns with the $\ell_{\text{cav}} = 1.142$ mm but leave out the pump wave for now. We apply an FFT to the longitudinal electric field over the spatial interval -0.75 mm $< x < 0.75$ mm, and the temporal interval 1 ns $< t <$ 69 ns. This produces the spectrum near the UH layer shown in figure 10. The figure shows a number of clearly separated peaks along the X-mode and EBW dispersion curves. The outer two curves are the EBW dispersion curves for right and left propagating waves, the dashed red line marks the left propagating wave. Transforming only into frequency at $x = 0$, we take note of the first several eigenfrequencies and plot them in figure 11 against our predictions using the geometry and our dispersion relations. The figure shows that lower order dispersion relations accurately predict only eigenfrequencies near the UH layer. Closer to the EC frequency, eigenfrequencies are off by several mode numbers and the trend is wrong. As an example, the mode at $m = 20$ corresponds to mode 16

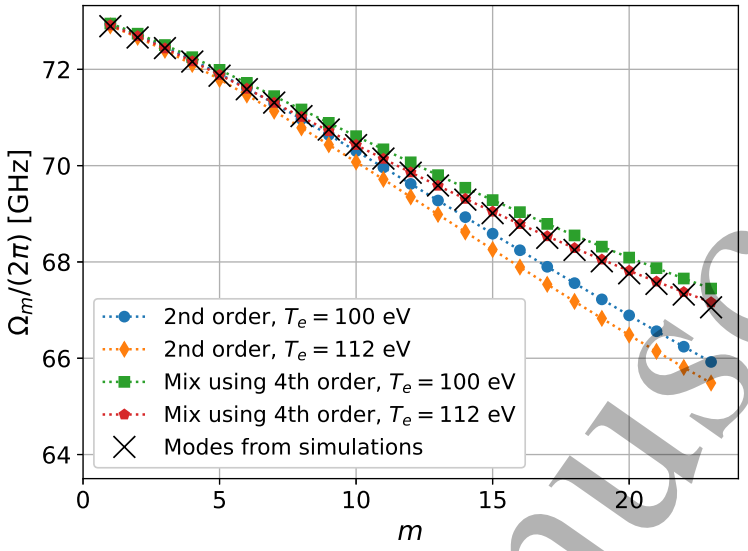

Figure 11. Eigenfrequencies of the $\ell_{\text{cav}} = 1.142$ mm cavity against mode number. The predictions are made using the dispersion relations in figure 2 and two different temperatures. All series agree at low mode numbers, where the wavenumbers are small and the asymptotic behavior is unnecessary. Curiously, the temperature appears to be a slightly elevated $T_e = 112$ eV.

or 17 using the lower order dispersion relations, and the blue and orange series have not started to flatten. The more accurate dispersion relation has the correct trend but is off by a small shift which appears to be remedied by increasing the temperature from 100 eV to 112 eV. Whilst this is not a great difference, EPOCH's outputted electron temperature remains much closer to the 100 eV used for the initial conditions. It is not possible to change the temperature for the lower order dispersion relation to obtain a better fit as the high mode number trend is incorrect. We will continue to use the $T_{\text{e}} = 112$ eV results from section 2 as the objective is to investigate TPD into eigenmodes and for this, we need to be able to predict the eigenmodes of a given cavity with good precision. We note that if these frequencies were observed in an experiment, either due to tunneling or recombination with a gyrotron[22], the characteristics of the cavity that traps them could in principle be determined by a fitting scheme similar to the temperature adjustment made based on figure 11.

3.3. Two plasmon decay instability

Having established that an eigenmode spectrum is present even without a pump wave, we pick an ℓ_{cav} such that $\sigma_m \approx 0$ by inspecting figure 6. Running a simulation both with and without the pump wave, the spectra in figure 12 are obtained. With the pump wave, two large peaks are found at the frequencies of the expected TPD daughter waves, i.e. at $\omega_1/(2\pi) = 70.141$ GHz and $\omega_2/(2\pi) = 69.859$ GHz. Comparing with the background level, i.e. without the pump wave, the peaks corresponding to the TPD daughter waves are far greater but the pump also lifts the general level of spectrum. To show that this

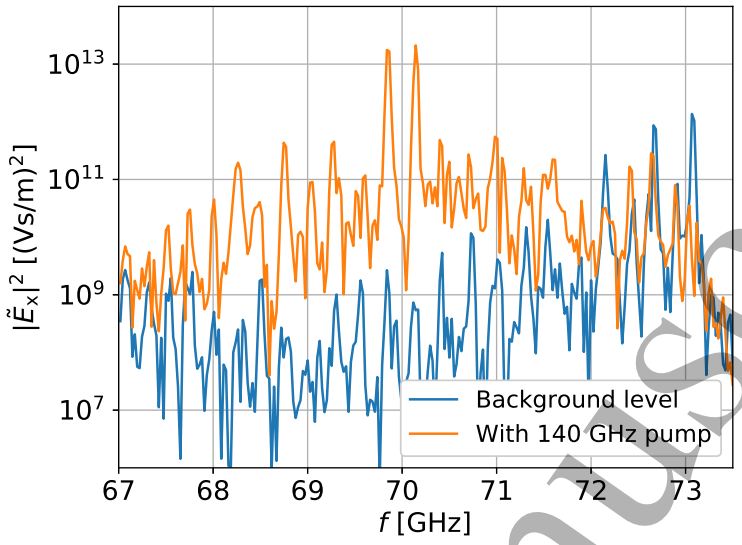

Figure 12. Example of a density profile where TPD daughter waves are close to eigenfrequencies at the center. In particular two peaks near 70 GHz are excited above the background level. The width of the density profile is $\ell_{\mathrm{cav}} = 1.142$ mm. The blue line is without a pump wave and the orange line has an $I_{\mathrm{pump}} = 1$ kW/mm^2 pump wave. The FFT window is 30 ns $< t <$ 69 ns. Note that the plot is semi logarithmic. In transformed space, the magnitude of the total pump wave is $|\tilde{E}_0|^2 \approx 3 \times 15$ (Vs/m)^2 and a longitudinal component of $|\tilde{E}_{0x}|^2 \approx 7 \times 12$ (Vs/m)^2 for comparison.

is not just a regular inhomogeneous PDI but that TPD into eigenmodes is essential, we now pick an ℓ_{cav} where $\sigma_m \approx 0.5$, which should result in a poor coupling to eigenmodes. The resulting spectra are shown in figure 13, and it is clear that the same TPD daughter waves are not present, which was the desired result. Comparing with the background spectrum, we see that the spectra are very similar with peaks at the same frequencies and of similar magnitudes. Some peaks in the background spectrum are slightly greater than the spectrum with the pump wave. We take from this that the spectra produced by EPOCH are stochastic to some degree.

Whilst we could have chosen ℓ_{cav} such that $\sigma_m \approx 1$, the twist in figure 13 is that this corresponds to a local minimum in σ_m using a lower order dispersion relation; see figure 6. Likewise, figure 12, in which the daughter waves are clearly visible, corresponds to a poor match using the lower order dispersion relation, which exemplifies the importance of precision when exciting the eigenmodes.

3.4. Structure size scan - growth rate and spectra

In the rest of this section, we scan ℓ_{cav}. As was argued in section 2, the eigenfrequency spectrum is uniquely determined by the plasma parameters and size of the non-monotonic density structure. By varying only the size of the cavity, i.e. the parameter ℓ_{cav}, we change the exact eigenfrequencies but not the selection rules for PDI at the center of the cavity. We expect the minima of σ_m and of σ_ω in figures 6 and 7 will be

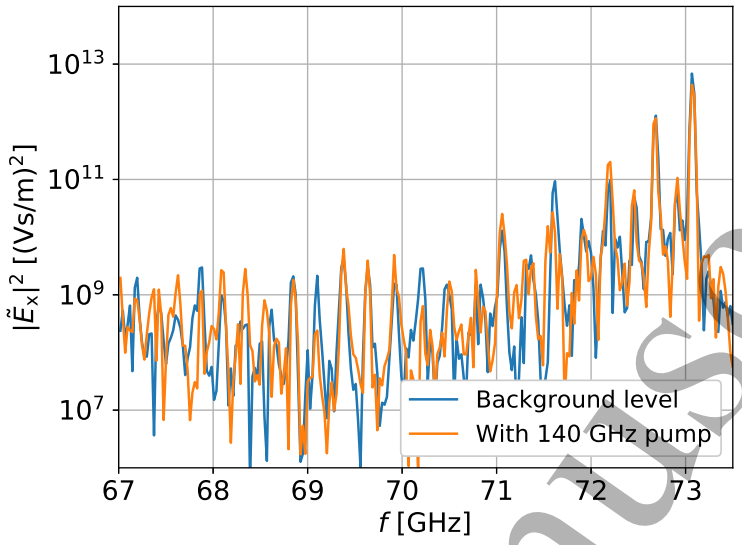

Figure 13. Example of a density profile where TPD daughter waves are far from eigenfrequencies at the center. No peaks are excited significantly above the background level. The width of the density profile with $\ell_{\mathrm{cav}} = 1.164$ mm. The blue line is without a pump wave and the orange line has an $I_{\mathrm{pump}} = 1$ kW/mm^2 pump wave. The FFT window is 30 ns $< t <$ 69 ns. Note that the plot is semi logarithmic. In transformed space, the magnitude of the total pump wave is $|\tilde{E}_0|^2 \approx 3 \times 15$ (Vs/m)^2 and a longitudinal component of $|\tilde{E}_{0x}|^2 \approx 7 \times 12$ (Vs/m)^2 for comparison.

optimal for exciting TPD daughter waves whereas the maxima will not. For each choice of ℓ_{cav}, we run a simulation both with and without an X-mode pump wave of intensity $I_{\mathrm{pump}} = 1$ kW/mm^2, corresponding roughly to the intensity in the center of a 1 MW gyrotron beam. We integrate the spectral power density from 69.5 GHz $< \omega/(2\pi) <$ 70.5 GHz, which includes the TPD daughter wave frequencies as well as some of the surrounding spectrum. The integral is dominated by the spectral peaks and should therefore give an indication of the intensity of the modes closest to $\omega_0/2$. This is used to determine the intensity of TPD daughter waves and the integrated spectral density from simulations without a pump is used as a measure of the error.

Figure 14 shows the result of the cavity size scan and it is clear that the TPD daughter wave population increases significantly near the the minima of σ_m. Near the maxima of σ_m, the integral drops to the level of the background noise. The overall shape is robust when changing the frequency integration range but the noise level is increased when more modes are included. The figure remains largely unaffected when using instead the maximum of the spectral power density in the same frequency range. The amplification of the background level for a convective PDI would correspond to $G_{\mathrm{obs}} = 8.27$ for $\ell_{\mathrm{cav}} = 1.142$ mm at the central red dotted line in figure 14. The convective amplification for a single pass at $I_{\mathrm{pump}} = 1$ kW/mm^2 was found to be just $G_4 = 1.20$. By inverting the expression for the amplification in equation (35), we find that the necessary pump electric field for a given amplification would be $|E_{\mathrm{necessary}}|^2 = [G_N/\delta_N]^{2N/(N+1)} v_{\mathrm{g},1} v_{\mathrm{g},2}/(|\nu_{12}\nu_{21}^*|\ell_{\mathrm{d},N}^2)$. Using the parameters of the

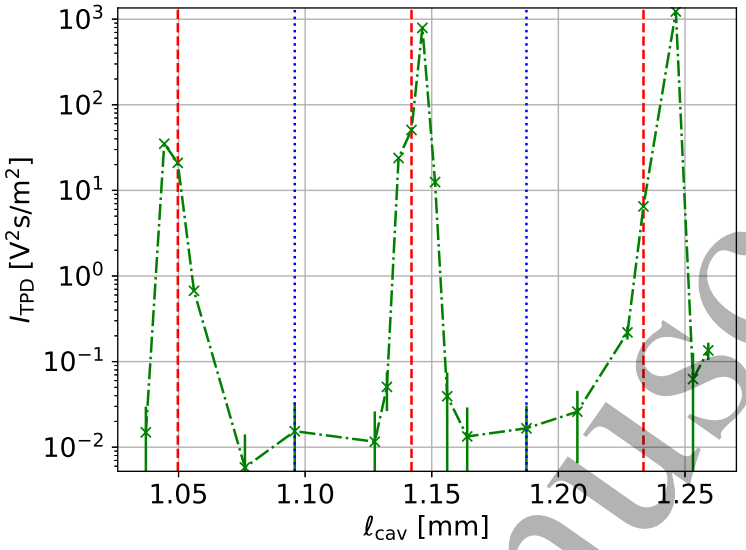

Figure 14. Integrated spectral density around TPD daughter frequencies for varying cavity size. The FFT window is 30 ns $< t <$ 69 ns and the integration range is 69.5 GHz $< \omega/(2\pi) <$ 70.5 GHz. The vertical red dashed lines mark sizes where σ_m has a local minimum and TPD would then couple well into eigenmodes. The vertical blue dotted lines are local maxima of σ_m and the coupling to eigenmodes is poor. The pump wave intensity is $I_{\mathrm{pump}} = 1$ kW/mm^2. There is good agreement with the predicted strong response only near the red dotted lines.

simulation, the corresponding intensity would be $I_{\mathrm{necessary}} = 22$ kW/mm^2, which is much greater than the input pump intensity. It is therefore clear that such amplification cannot simply be due to a convective PDI which amplifies the daughter waves during just one pass through the decay region.

The peaks in figure 14 tend to be found next the predicted peaks and the largest peak is the rightmost one in the figure even though the central peak takes the smallest value of σ_m. Perhaps the increasing size of the decay region and smaller mode separation with greater ℓ_{cav} makes up for the slightly larger σ_m. In principle the PDI may also not be taking place exactly in the center of the cavity. This would mean that the selection rules instead are satisfied in two places, each with a smaller decay region. However, the sum of two smaller decay region could add up to a larger total decay region. Still, the results from the parameter scan agree very well with the prediction. Lastly, by comparing the central peak in figure 14 to σ_ω in figure 7, we find that the TPD daughter waves experience amplification to a level much greater than the background level when $\sigma_\omega/(2\pi) < (0.06 \pm 0.03)$ GHz. With this requirement on σ_ω, the example of a larger $\ell_{\mathrm{cav}} \approx 8$ mm structure similar to blob sizes in ASDEX Upgrade would see growth in most cases as $\sigma_\omega/(2\pi) \lesssim 0.04$ GHz. However, the σ_ω tolerance is likely to depend on the spatial profile of the plasma parameters.

Next, we evaluate the growth rates by setting up a moving FFT window of length 20 ns, starting at 1 ns and moving in steps of 6.7 ns. We integrate the same frequency interval of 69.5 GHz $< \omega/(2\pi) <$ 70.5 GHz for all of the resulting spectral power densities

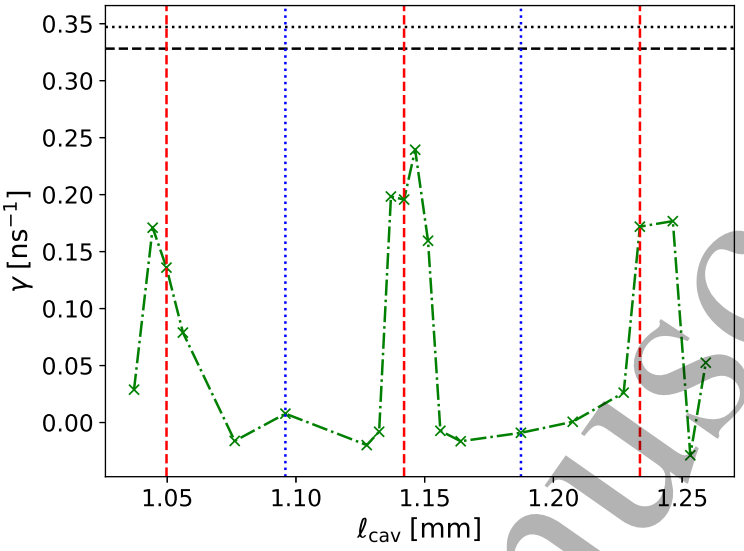

Figure 15. TPD daughter wave growth rates from simulations in figure 14. Data points are removed when a growth rate could not be established with a simple exponential fit, e.g. because the growth due to TPD is too weak compared to the background noise. The vertical dashed red lines correspond to minima in σ_m whereas the vertical dotted blue lines are maxima. The horizontal dashed and dotted black lines mark the predicted PDI growth rates γ_1 and γ_2 respectively, as calculated in section 2. The pump wave intensity is $I_{\mathrm{pump}} = 1$ kW/mm^2. The peak growth rates are comparable to the predicted growth rates.

and fit a function of the form $\phi(t) = \phi_0 \exp(\gamma t) + \phi_{\mathrm{background}}$ to the time evolution of the integrated spectra in the initial exponential growth phase. We perform the same treatment on the simulations without a pump and subtract the found growth rates from those of the simulations with a pump wave. The spectral level drops off in the absence of a pump wave. This is likely because the waves that are excited in the initialization of the simulations experience losses such as tunneling out of the cavity. Figure 15 shows the fitted γ as a function of the cavity size ℓ_{cav}. Again, we see growth when σ_m is small and the features of the three peaks are mostly similar to figure 14. The growth rates obtained in the simulations are smaller than the estimated growth rates γ_1 and γ_2 marked by the horizontal dashed and dotted lines. Still, the growth rates are comparable to the peak values near σ_m is small and the model applies best. The prediction can perhaps be improved using only kinetic theory, such as in [44], instead of the part kinetic and part cold fluid result presented in section 2. It is also possible that a better agreement can be found by changing the FFT window size and perhaps even more so if the parameters were chosen such that growth rates were smaller and simulations were longer. Nevertheless, we note that using the mobility tensor derived from kinetic theory did improve the estimate over that using the cold fluid mobility tensor. Furthermore, with a gain of merely $G_4 = 1.20$ at a single pass, which takes on the order of 1 ns for the daughter waves to complete, the exponential growth cannot be explained as simply a convective PDI in an inhomogeneous medium without the trapping. The points found near the

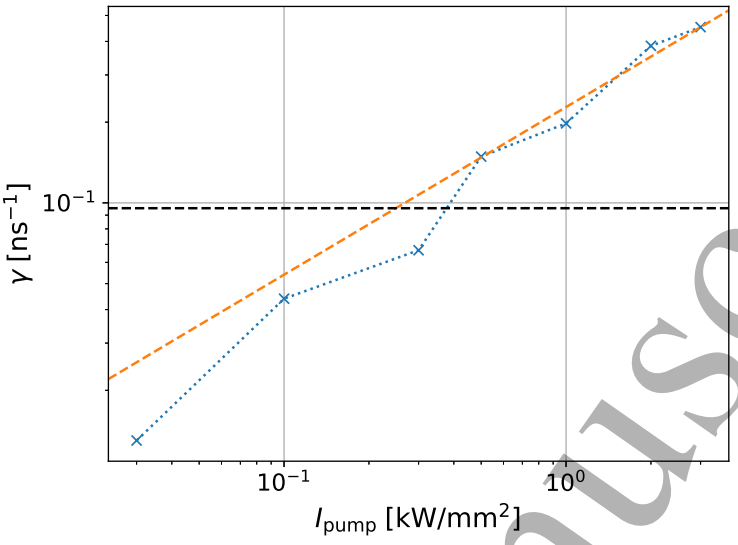

Figure 16. TPD daughter wave growth rate against pump wave intensity for a cavity size of $\ell_{\text{cav}} = 1.142$ mm. Growth rates are estimated by integrating the longitudinal spectral density over the range 69.5 GHz $< \omega/(2\pi) <$ 70.5 GHz and fitting an exponential function. The vertical orange dashed line is an $I_{\text{pump}}^{5/8}$ trend line and the horizontal black dashed line is the level of the negative growth rate of the simulation without a pump wave, which has been subtracted from all points. The black line is essentially the threshold for the instability. Note that both axes are logarithmic.

vertical blue dotted lines fluctuate around zero because the growth rates are similar to that of the simulations without a pump wave. Although, the growth rate estimate presented in 2 is a reasonable starting point, there are certainly ways to improve it. In particular, the model does not include any self-interaction that could explain why only eigenmodes survive several round trips. Including self-interaction may alter the growth rate, but theory developed for optical cavities[45] using the Ginzburg-Landau equation or the nonlinear Schrödinger equation usually rely on homogeneous media bounded by mirrors, which is difficult to apply to the case of trapped UH waves. Still, the found growth rates are on the order of the predicted growth rates, which is a strong indication that an absolute PDI is taking place. We note that doubling the number of superparticles for the simulation does not significantly affect the obtained growth rate for $\ell_{\text{cav}} = 1.142$ mm, suggesting that the small discrepancy in growth rates is not due to under sampling of the electron distribution function.

Lastly, we investigate how the growth rate scales with the pump intensity. Using the same FFT windows of length 20 ns, starting at 1 ns and in steps of 6.7 ns, we run simulations of $\ell_{\text{cav}} = 1.142$ mm with different pump intensities. The result is shown in figure 16 along with a $G_4/\tau_j \propto I_{\text{pump}}^{5/8}$ trend indicated by the orange dashed line. This particular trend comes from equation (35). The black dashed line is the instability threshold as it marks the level of the negative growth of the simulations without a pump. Above this threshold, the trend is close to the prediction. Below the threshold, the trend appears to follow a slightly higher power of I_{pump}, i.e. it is not closer to the

homogeneous $I_{\text{pump}}^{1/2}$ trend. The main contributing mechanisms to this threshold are loss of the eigenmodes due to tunneling and damping. In particular the small cavity size and steep density gradients mean that the conversion at the turning points is not complete. Although we can estimate a growth rate for the simulations below the threshold by comparing them to the background simulation, we note that they are rather noisy and difficult to fit an exponential trend to at times. The highest intensity simulations, on the other hand, grow rather quickly compared to FFT windows, which means that the growth rate in even higher intensity simulations would be hard to determine using this method.

The primary daughter waves do not continue to growth forever following the rates in figures 15 and 16. For the $\ell_{\text{cav}} = 1.142$ mm and $I_{\text{pump}} = 1$ kW/mm^2 simulation, the primary daughter wave populations saturate after approximately 70 ns. From this point, the populations of other eigenmodes increase and scattering at frequencies shifted from the pump by approximately the lower hybrid frequency is increased by orders of magnitude, a feature resembling observations in [14, 15]. This is expected to be caused by subsequent PDIs, which drain the primary daughter waves instead of the injected wave at ω_0.

The growth rates presented in figures 15 and 16 are higher than one would expect from a blob of similar size in a tokamak fusion plasma as only a direction perpendicular to the magnetic field is included here. One of the main loss mechanism of the trapped UH eigenmodes in plasma experiments is along the magnetic field lines due to diffraction.

4. Discussion and Conclusion

Using a fully kinetic PIC code, we have demonstrated that non-monotonic plasma density structures can act as cavities and give rise to trapped UH waves which form eigenmodes that satisfy a quantization condition. Our simulations show that the eigenmodes of such cavities can be excited through PDIs of an electromagnetic X-mode pump wave passing through the cavity. This could be the case of an ECRH gyrotron beam passing through a density perturbation such as a blob or a magnetic island in a magnetically confined fusion plasma. More importantly, we show that UH waves are not excited through PDIs inside the cavity unless the PDI selection rules are satisfied for decay into eigenmodes of the cavity.

We have derived a closed and numerically tractable expression for the X-mode and EBW dispersion relation which approximates the full expression well, both near the UH layer and near the EC resonance. The precision of the expression allows us to predict the eigenfrequencies quickly and map out in which geometries we can expect to see PDIs exciting eigenmodes. We furthermore generalized the expression for amplification of daughter waves in a convective PDI to account for a decay region where the first several derivatives of the plasma parameters vanish. This showed that the amplification due to convective PDI for a single pass was insufficient to explain the observed growth of certain eigenmodes. By applying an electron mobility tensor derived from kinetic

theory, we were able to improve our estimated PDI growth rate which was comparable to that of the simulations as well as the homogeneous PDI. This confirms that the trapping mechanism provided by the non-monotonic structure gives rise to an absolute instability.

The eigenfrequency separation is affected by several plasma parameters including the geometry of the non-monotonic structure. Whilst the plasma parameters used here could be realized in e.g. the tokamak ASDEX Upgrade or the stellarator Wendelstein 7-X, the cavity width is small compared to the typical blob size in those machines. This means that the eigenfrequency separation can be expected to be smaller than in our simulation and consequently, it is easier to satisfy selection rules for PDIs into eigenmodes, both in small blobs and, of course, in large islands. Eigenmodes in the small structures presented in this article suffer from comparably large losses due to tunneling but nevertheless demonstrate how a non-monotonic plasma density structure can facilitate absolute PDIs and significantly reduce PDI thresholds. When calculating further decay cascades that would produce experimentally observable scattering escaping the cavity, eigenmodes must be taken into account for each step of the cascade in the same manner as was presented in this article for the primary decay.

5. Acknowledgments

This work has been supported by research grant 15483 from VILLUM FONDEN and the Enabling Reseach grant ENR-MFE19.DTU-03 from the EUROfusion Consortium. The work has been carried out within the framework of the EUROfusion Consortium and has received funding from the Euratom research and training programme 2014-2018 and 2019-2020 under grant agreement No 633053. The views and opinions expressed herein do not necessarily reflect those of the European Commission. The authors thank Søren "Sauron" Kjer Hansen for private communications.

References

[1] A A Sukhorukov *et al* 2000 Physical Review E **63**, 016615
[2] M Faraday Philos. Trans. R. Soc. London **121**, 319 (1831)
[3] C M Topaz *et al* 2004 Physical Review E **70**, 066206
[4] V P Silin 1965 Sov. Phys. JETP **21** 1127
[5] Y M Aliev *et al* 1966 Sov. Phys. JETP **23** 626
[6] T Amano *et al* 1969 J. Phys. Soc. Japan **26** 529
[7] A D Piliya 1971 Proc. 10th Int. Conf. Phenomena in Ionized Gases (Oxford) ed R N Franklin (Oxford: Donald Parsons & Co. Ltd) p 320
[8] M N Rosenbluth 1972 Phys. Rev. Lett. **29** 565
[9] A D Piliya 1973 ZhETF. Pis. Red. **17** 374
[10] H P Laqua 2007 Plasma Phys. Control. Fusion, **49** R1
[11] R B White *et al* 1974 Plasma Physics **16** 565-587
[12] F S McDermott *et al* 1982 Phys. Fluids **25** 1488
[13] R Wilhelm, V Erckmann, G Janzen, W Kasparek, G Müller, E Räuchle, P G Schüller, K Schwörer and M Thumm 1984 Plasma Phys. Control. Fusion, **26** 1433

[14] E Westerhof *et al* 2009 Phys. Rev. Lett. **103** 125001
[15] S K Nielsen *et al* 2013 Plasma Phys. Control. Fusion **55** 115003
[16] E Z Gusakov *et al* 2009 AIP Conference Proceedings **1187**, 645
[17] E Z Gusakov *et al* 2011 Nucl. Fusion **51** 073028
[18] A Yu Popov *et al* Plasma Phys. Control. Fusion **57**, 025022 (2015)
[19] A Yu Popov *et al* 2015 Journal of Experimental and Theoretical Physics, vol. 121, No. 2, pp. 362-374
[20] E Z Gusakov *et al* Physics of Plasmas **23**, 082503 (2016)
[21] E Z Gusakov *et al* Physics of Plasmas **25** (2018) 062106
[22] E Z Gusakov *et al* Nucl. Fusion **59** (2019) 104003
[23] S K Hansen PhD thesis *Parametric Decay Instabilities in the Electron Cyclotron Resonance Heating Beams at ASDEX Upgrade*, 31 August 2019
[24] A B Altukhov, V I Arkhipenko, A D Gurchenko, E Z Gusakov, A Yu Popov, L V Simonchik and M S Usachonak 2019 EPL **126** 15002
[25] V. F. Andreev, Yu. N. Dnestrovskij, M. V. Ossipenko, K. A. Razumova and A. V. Sushkov Plasma Physics and Controlled Fusion **46** (2004) 319-335
[26] D G Bulyginskii, V V Dyachenko, M A Irzak, M M Larionov, L S Levin, G A Serebrenyi and N V Shustova Sov. J. Plasma Phys. Vol. 12, pp. 77-80 (1986)
[27] Z A Pietrzyk, A Pochelon, R Behn, A Bondeson, M Dutch, T P Goodman, M Q Tran and D R Whaley 1993 Nucl. Fusion **33** 197
[28] M G Senstius *et al* Phys. Plasmas **27**, 062102 (2020)
[29] D. G. Swanson 2003 *Plasma waves* 2nd edn (Boca Raton, FL: CRC Press)
[30] M. Abramowitz and I. A. Stegun 1972 *Handbook of mathematical functions* 10th printing (National Bureau of Standards, Washington D. C.)
[31] S. L. Shmakov International Journal of Pure and Applied Mathematics (2011) **71**, 2, 251
[32] U. Neuner *et al* Nuclear fusion **61** (2021) 036024
[33] A. K. Ram *et al* 2000 Phys. Plasmas **7**, 4084
[34] S.K. Hansen, S.K. Nielsen, J. Stober, J. Rasmussen, M. Stejner, M. Hoelzl, T. Jensen and the ASDEX Upgrade team Nuclear Fusion **60** (2020) 106008
[35] E. Z. Gusakov and V. I. Fedorov 1979 Soviet Journal of Plasma Physics **5** 463-6
[36] M. Porkolab an B. I. Cohen 1988 Nuclear Fusion **28** 239
[37] G. Fuchert, G. Birkenmeier, D. Carralero, T. Lunt, P. Manz, H. W. Müller, B. Nold, M. Ramisch, V. Rohde, U. Stroth, and the ASDEX Upgrade Team Plasma Physics and Controlled Fusion **56** (2014) 125001
[38] K. G. Budden 1961 *Radio waves in the ionosphere* (Cambridge University Press)
[39] N. A. Lopez and A. K. Ram Plasma Physics and Controlled Fusion **60** (2018) 125012
[40] T D Arber *et al* Contemporary particle-in-cell approach to laser-plasma modelling Plasma Phys. Control. Fusion **57** (2015) 113001
[41] M G Senstius *et al* Plasma Phys. Control. Fusion **62** (2020) 025010
[42] A. V. Arefiev *et al* 2017 Nucl. Fusion **57** 116024
[43] A. Taflove and S. C. Hagness 2000 *Computational Electrodynamics: The Finite-Difference Time-Domain Method* (Artech House) 2nd edition
[44] E. Z. Gusakov, A. Yu. Popov and P. V. Tretinnikov Plasma Physics and Controlled Fusion**61** (2019) 085008
[45] A. M. Perego, S. V. Smirnov, K. Staliunas, D. V. Churkin and S. Wabnitz Physical Review Letters **120**, 213902 (2018)